JACS
JOURNAL OF THE AMERICAN CHEMICAL SOCIETY
Article
pubs.acs.org/JACS

The Role of Regioregularity, Crystallinity, and Chain Orientation on Electron Transport in a High-Mobility n-Type Copolymer

Robert Steyrleuthner,[†] Riccardo Di Pietro,[†] Brian A. Collins,[‡] Frank Polzer,[§] Scott Himmelberger,[∥] Marcel Schubert,[†] Zhihua Chen,[⊥] Shiming Zhang,[⊥] Alberto Salleo,[∥] Harald Ade,[#] Antonio Facchetti,*[,⊥] and Dieter Neher*[,†]

[†]Institut für Physik und Astronomie, Universität Potsdam, Karl-Liebknecht-Str. 24-25, 14476 Potsdam, Germany

[‡]Materials Science and Engineering Division, National Institute of Standards and Technology, 100 Bureau Drive, Gaithersburg, Maryland 20899, United States

[§]Institut für Physik, Humboldt-Universität zu Berlin, Newtonstraße 15, 12489 Berlin, Germany

[∥]Materials Science and Engineering, Stanford University, 496 Lomita Mall, Stanford, California 94305-4034, United States

[⊥]Polyera Corporation, 8045 Lamon Avenue, Suite 140, Skokie, Illinois 60077-5318, United States

[#]Department of Physics, North Carolina State University, 2401 Stinson Drive, Raleigh, North Carolina 27695, United States

Supporting Information

ABSTRACT: We investigated the correlation between the polymer backbone structural regularity and the charge transport properties of poly{[*N*,*N*′-bis(2-octyldodecyl)-1,4,5,8-naphthalenediimide-2,6-diyl]-*alt*-5,5′-(2,2′-bithiophene)} [P(NDI2OD-T2)], a widely studied semiconducting polymer exhibiting high electron mobility and an unconventional micromorphology. To understand the influence of the chemical structure and crystal packing of conventional regioregular P(NDI2OD-T2) [RR-P(NDI2OD-T2)] on the charge transport, the corresponding regioirregular polymer RI-P(NDI2OD-T2) was synthesized. By combining optical, X-ray, and transmission electron microscopy data, we quantitatively characterized the aggregation, crystallization, and backbone orientation of all of the polymer films, which were then correlated to the electron mobilities in electron-only diodes. By carefully selecting the preparation conditions, we were able to obtain RR-P(NDI2OD-T2) films with similar crystalline structure along the three crystallographic axes but with different orientations of the polymer chains with respect to the substrate surface. RI-P(NDI2OD-T2), though exhibiting a rather similar LUMO structure and energy compared with the regioregular counterpart, displayed a very different packing structure characterized by the formation of ordered stacks along the lamellar direction without detectible π-stacking. Vertical electron mobilities were extracted from the space-charge-limited currents in unipolar devices. We demonstrate the anisotropy of the charge transport along the different crystallographic directions and how the mobility depends on π-stacking but is insensitive to the degree or coherence of lamellar stacking. The comparison between the regioregular and regioirregular polymers also shows how the use of large planar functional groups leads to improved charge transport, with mobilities that are less affected by chemical and structural disorder with respect to classic semicrystalline polymers such as poly(3-hexylthiophene).

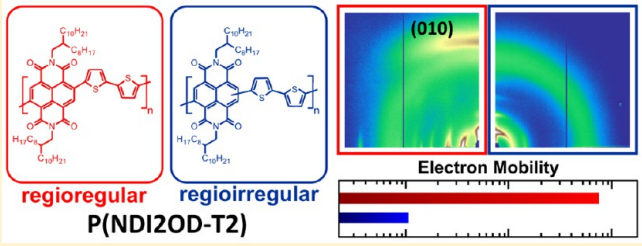

INTRODUCTION

The development of high-mobility semiconducting polymers requires a thorough understanding of the interplay between the molecular structure and the solid-state packing and how they affect the solid-state charge transport properties.[1−6] Initial pioneering studies on alkyl-substituted polythiophenes demonstrated that tuning the substitution type and degree of regioregularity, enhanced intramolecular π-conjugation, increased intermolecular $\pi-\pi$ interactions, and degree of crystallinity can substantially improve charge transport, with mobilities increasing by several orders of magnitude for highly ordered polymers.[7−14] On the other hand, the recent development of low-band-gap polymers comprising alternating donor and acceptor (D−A) units in the backbone led to an improvement in the charge transport properties, with field-effect mobilities in the range of 1 $cm^2\ V^{-1}\ s^{-1}$, despite the fact that several of these polymers show a less ordered packing structure.[15−19] This seemingly contradictory result was primarily ascribed to the employed functional D−A units which, by promoting core planarization and intermolecular $\pi-\pi$ interactions, compensate for the reduced order in the corresponding thin films.[20,21]

Received: November 28, 2013
Published: February 14, 2014

   dx.doi.org/10.1021/ja4118736 | *J. Am. Chem. Soc.* 2014, 136, 4245−4256

In this respect, regioregular poly{[*N*,*N*′-bis(2-octyldodecyl)-1,4,5,8-naphthalenediimide-2,6-diyl]-*alt*-5,5′-(2,2′-bithiophene)} [RR-P(NDI2OD-T2)], an electron-transporting polymer comprising a naphthalenediimide acceptor and a dithiophene donor units, is a very interesting system for studying the correlation between molecular and solid-state structure and charge transport in donor−acceptor copolymers. Since its introduction in 2009,[22] RR-P(NDI2OD-T2) has been widely investigated thanks to its facile processability and remarkable electronic properties.[23−25] A thorough characterization of this polymer revealed a rather unique film microstructure displaying small but well-ordered crystallites having polymer chains with a face-on orientation in the bulk of the film, and with the top surface showing an edge-on configuration.[26,27] This particular morphology allows good electron transport properties in both vertical diodes and field-effect transistors.[23,28−31] In a recent publication, we also showed that this polymer has a strong tendency to form well-ordered aggregates in several common organic solvents and that the aggregation strongly affects the solution and bulk optical properties.[32] Control of the preaggregation proved to be essential for the optimization of organic solar cells in which P(NDI2OD-T2) acts as the electron-accepting component.[33−37]

In an effort to understand the origin of the good transport properties of this material, Rivnay and co-workers showed that melt-annealing of the polymer film allows the polymer chain orientation in the bulk of the film to be changed from primarily face-on to edge-on, leading to a corresponding decrease in vertical electron conductivity,[38] while Schuettfort et al. showed that the top surface is unaffected by the change in bulk orientation.[27] The strong tendency of the polymer to form ordered thin-film microstructures under a wide range of processing conditions limits the possibility to analyze and separate the influence of the polymer molecular structure versus film crystallization on the electron transport properties.

In this contribution, we show the impact of several structural parameters on the electron transport of NDI-based polymers by separately tuning the chain orientation, degree of crystallinity along the different directions, and degree of aggregation of the polymer chains. To achieve this goal, we synthesized for the first time a regioirregular (RI) derivative of P(NDI2OD-T2) in which the NDI−T2 linkage is random at the 2,6- and 2,7-positions of NDI. In contrast to poly(3-alkylthiophene)s such as poly(3-hexylthiophene) (P3HT),[39,40] the regioirregular linkage does not vary the intramolecular steric demand of the backbone versus the RR isomer, allowing the RI polymer to exhibit similar absorption features and LUMO energy as its RR counterpart, as shown by electrochemical and optical measurements. However, we will show that while aggregation is reduced, the RI polymer exhibits a rather unique microstructure comprising large, two-dimensionally ordered domains developed along the lamellar stacking and polymer backbone direction without detectible π-stacking. This result is in striking contrast to homopolymers such as P3HT, where the regioirregular linkage leads to an amorphous film with no evidence of ordering.[41] This unique feature provides us with an ideal test bench to separately study the role of ordering along the different crystallographic axes on the charge transport properties. Using either chlorobenzene, which strongly promotes aggregation in solution, or a 1:1 (v/v) chloronaphthalene:xylene mixture, which instead inhibits aggregation, we were able to vary both the degree of crystallinity of RR-P(NDI2OD-T2) films and the orientation of the polymer chains with respect to the substrate surface while keeping a similar thermal history.[32] All of the structural properties of the films were accessed by grazing-incidence X-ray diffraction (GIXD) and transmission electron microscopy (TEM), demonstrating the role of solution preaggregation in the formation of well-ordered crystallites.

Finally, electron-only devices were fabricated with films of RR- and RI-P(NDI2OD-T2). This provided us with the opportunity to explore the structure−charge transport correlations, demonstrating charge transport anisotropy between the lamellar and π-stacking directions. The rather high bulk electron mobility of RI-P(NDI2OD-T2) films demonstrates the role of the chemical structure of the polymer chains in improving the interchain electron transfer despite the poor packing registry along the π-stacking direction. Moreover, the comparison of RR- and RI-P(NDI2OD-T2) provides a direct experimental proof of the correlation between crystallization along the π-stacking direction and improved charge transport and the negligible influence of crystallization along the lamellar stacking direction on charge transport due to the insulating nature of the solubilizing side chains.

EXPERIMENTAL SECTION

Materials and Reagents. The reagents were purchased from commercial sources and used without further purification, unless otherwise noted. 2-Octyldodecylamine[42] and 5,5′-bis-(trimethylstannyl)-2,2′-bithiophene[43] were prepared according to literature procedures. Regioregular P(NDI2OD-T2) polymer[44] is now commercially available from Polyera Corporation under the trade name of ActivInk N2200. NMR spectra were obtained using an Inova 500 (500 MHz) NMR spectrometer. Elemental analyses were performed by Midwest Microlab, LLC. Polymer molecular weights were determined on a Waters gel-permeation chromatography (GPC) system (Waters Pump 510) in tetrahydrofuran (THF) at room temperature versus polystyrene standards.

Preparation of 2,3,6,7-Tetrabromonaphthalene-1,4,5,8-tetracarboxylic Dianhydride (NDA-Br_4).[45] A mixture of 1,4,5,8-naphthalenetetracarboxylic dianhydride (NDA) (2.8 g, 10.3 mmol) and oleum (20% SO_3, 100 mL) was stirred at 55 °C for 2 h. A solution of dibromoisocyanuric acid (DBI) (6.0 g, 21.0 mmol) in oleum (50 mL) was then added over the course of 40 min. The resulting mixture was then warmed to 85 °C and maintained at this temperature for 50 h. Upon cooling to room temperature, the reaction mixture was poured onto crushed ice (500 g). This mixture was diluted with water (500 mL) and then stirred at room temperature for 1 h. The precipitates were collected by centrifuge, washed with water and methanol, and dried under vacuum, leading to a greenish-yellow solid (6.3 g). This material was used for next step without further purification. Elemental Analysis (EA) (mass %) Calcd: C, 39.47; H, 0.47; N, 0.00. Found: C, 38.20; H, 0.79; N, 0.00.

Preparation of *N*,*N*′-Bis(2-octyldodecyl)-2,3,6,7-tetrabromonaphthalene-1,4,5,8-bis(dicarboximide) (NDI2OD-Br_4). A mixture of NDA-Br_4 (2.34 g, 5.49 mmol), 2-octyldodecylamine (4.10 g, 13.78 mmol), *o*-xylene (18 mL), and propionic acid (6 mL) was stirred at 140 °C for 2 h. After the mixture was cooled to room temperature, most of solvents were removed in vacuo, and the residue was purified by column chromatography on silica gel with a 1:1 (v/v) chloroform:hexane mixture as the eluent, affording a slightly yellow solid as the product (1.98 g, 2.01 mmol, 96.7% yield). ^{1}H NMR ($CDCl_3$ 500 MHz): δ 4.13 (d, J = 7.5 Hz, 4H), 1.96 (m, 2H), 1.19−1.43 (m, 64H), 0.85−0.90 (m, 12H). EA (mass %) Calcd: C, 65.84; H, 8.60; N, 2.84. Found: C, 65.68; H, 8.60; N, 2.89.

Preparation of *N*,*N*′-Bis(2-octyldodecyl)-2,6- and -2,7-dibromonaphthalene-1,4,5,8-bis(dicarboximide) (NDI2OD-2,6Br_2/NDI2OD-2,7Br_2 Mixture). A mixture of NDI2OD-Br_4 (2.27 g, 1.98 mmol) and Zn powder (0.32 g, 4.95 mmol) in isopropyl alcohol (IPA)

dx.doi.org/10.1021/ja4118736 | J. Am. Chem. Soc. 2014, 136, 4245−4256

(120 mL), AcOH (10 mL), and water (5 mL) was refluxed overnight under nitrogen. After the mixture was cooled to room temperature, most of the solvents were removed in vacuo, and the residue was dissolved in chloroform (~150 mL). This solution was washed with $NaHCO_3$ aqueous solution, dried over $MgSO_4$, and concentrated in vacuo. The resulting crude material was first purified by column chromatography (silica gel, 2:1 v/v dichloromethane:hexanes) to give a mixture of the 2,6 and 2,7 isomers, which was further purified by three recrystallizations from IPA to afford a yellow solid (0.71 g, 49% yield). ^{1}H NMR ($CDCl_3$ 500 MHz): δ 9.01 (s, 0.68H), 8.97 (s, 0.53H), 4.16 (m, 4H), 1.97 (m, 2H), 1.20−1.40 (m, 64H), 0.84−0.89 (m, 12H). ^{13}C NMR (CDCl3): δ 161.7, 161.5 161.3, 161.1, 139.1, 128.9, 128.6, 128.5, 127.9, 127.7, 125.4, 124.2, 45.6, 36.6, 32.1, 32.0, 31.7, 30.2, 29.9, 29.8, 29.7, 29.6, 29.5, 26.5, 22.9, 22.8, 14.3. EA (mass %) Calcd: C, 65.84; H, 8.60; N, 2.84. Found: C, 65.64; H, 8.55; N, 2.77.

Preparation of Poly{[*N*,*N*′-bis(2-octyldodecyl)-1,4,5,8-naphthalenediimide-2,6- and -2,7-diyl]-*alt*-5,5′-(2,2′-bithiophene)} [RI-P(NDI2OD-T2)] . Under argon, the NDI2OD-2,6Br_2/NDI2OD-2,7Br_2 mixture (88.4 mg, 0.090 mmol), 5,5′-bis(trimethylstannyl)-2,2′-bithiophene (38.4 mg, 0.078 mmol), and $Pd(PPh_3)_2Cl_2$ (2.7 mg, 0.0038 mmol) were dissolved in anhydrous toluene (10 mL), and the solution was stirred at 90 °C for 18 h. Bromobenzene (0.5 mL) was then added, and the reaction mixture was maintained at 90 °C for an additional 5 h and then cooled to room temperature. A solution of potassium fluoride (1.2 g) in water (2.4 mL) was added. This mixture was stirred at room temperature for 1 h before it was extracted with chloroform (150 mL). The organic layer was washed with water (100 mL × 2), dried over anhydrous sodium sulfate, and concentrated on a rotary evaporator. The residue was taken up with chloroform (15 mL) and precipitated in methanol (100 mL) and acetone (100 mL) in sequence. The obtained blue solid product was purified by Soxhlet extraction with acetone for 48 h. The remaining solid residue was redissolved in chloroform (20 mL), and the resulting mixture was heated to boiling. Upon cooling to room temperature, the chloroform solution was filtered through a 5 μm filter, and the filtrate was added slowly to methanol (100 mL). The precipitates were collected by filtration, washed with methanol, and dried in vacuum, leading to a deep-blue solid as the product (75 mg, 97.1% yield). ^{1}H NMR ($CDCl_2CDCl_2$, 500 MHz): δ 8.70−8.90 (br m, 2H), 7.20−7.50 (br m, 4H), 4.11 (br s, 2H), 2.00 (br s, 4H), 1.10−1.46 (br m, 64H), 0.76−0.89 (br m, 12H). GPC: M_n = 28.6 kg/mol, M_w = 88.5 kg/mol, PDI = 3.1. EA (mass %) Calcd: C, 75.26; H, 8.96; N, 2.83. Found: C, 75.24; H, 8.60; N, 2.72.

Device Preparation and Characterization. P(NDI2OD-T2) was dissolved overnight at 60 °C using either chlorobenzene or a 1:1 chloronaphthalene:xylene mixture (different concentrations were used to obtain layers with different thicknesses). All of the films analyzed in this work were spin-coated in a nitrogen atmosphere at 1000 rpm for 30 s and rapidly transferred to a vacuum oven, where they were dried at room temperature for 10 min. These films were either measured as such or annealed in nitrogen for 10 min at 200 °C. Samples for optical spectroscopy were spin-coated on solvent-cleaned glass (Carl Roth microscope slide 0656.1). GIXD samples were prepared on silanized doped silicon substrates with only a native oxide coating. Samples for TEM were prepared on poly(styrenesulfonic acid)-coated glass and floated onto TEM grids in deionized water. Electron-only devices were prepared by thermal evaporation of 2 nm Cs_2CO_3 at 0.1 Å/s on structured indium tin oxide (ITO) (100 nm thickness and 15 Ω sheet resistance) at a base pressure below 2×10^{-6} mbar and subsequent spin-coating of the respective P(NDI2OD-T2) film in a glovebox atmosphere. To finalize the diode structure, we applied 1 nm Cs_2CO_3 and 100 nm aluminum (5 Å/s) as a top contact. Current−voltage characteristics were measured inside the glovebox using a computer-controlled Keithley 2400 source/measure unit.

Electrochemistry and Optical Absorption. Electrochemical measurements were performed on thin polymer films using a CH Instruments model 660A electrochemical workstation with a three-electrode cell configuration (VC-2 voltammetry cell). The solvent was dry THF containing 0.1 M tetra-*n*-butylammonium hexafluorophosphate as the electrolyte. A 1.0 mm diameter platinum disk electrode, a platinum wire counter electrode, and a Ag/Ag_xO reference electrode were employed. Ferrocene/ferrocenium (Fc/Fc^+) was used as an internal reference for all measurements, and the potential values obtained in reference to the silver electrode were converted to the saturated calomel electrode (SCE) scale (Fc/Fc^+ = 0.54 V vs SCE). Thin films were deposited onto the working electrode by drop-casting a solution of the polymer sample in chloroform. The optical absorption spectra of thin films (~30 nm on glass) were taken with a Cary 5000 spectrometer equipped with an integrating sphere.

Grazing-Incidence X-ray Diffraction. Measurements were performed at beamline 7.3.3 of the Advanced Light Source (beam energy of 10 keV and beam width of ~1 mm).[46] A Pilatus 1M photon-counting detector array was used to measure diffraction intensities. Most of the X-ray flight path was contained by a helium atmosphere to reduce air scatter in the signal. The edges of the 2.5 cm × 2.5 cm substrates were cleaved to eliminate diffraction signal from the edge of the spin-cast film, leaving approximately the center 1 cm × 1 cm of the film. Diffraction intensities were acquired at an incident angle just above the film critical angle (measured to be $\alpha_C \approx 0.10°$ for RR and $\alpha_C \approx 0.12°$ for RI) to obtain the maximum diffraction signal and at an incident angle well above the critical angle of the substrate ($\alpha = 0.20°$), where the intensity was a linear function of the illuminated film volume. The results from analysis of the measurements at the critical angle are presented here with their intensities scaled to those measured at the high incident angle. The intensities were additionally corrected for beam footprint (length of the sample in the beam) and film thickness.

Pole figures were constructed by integrating the intensities at each detector azimuth within a q range encompassing the diffraction peak and subtracting a linear background defined by the intensities at either end of the integrated q range. Additionally, the detector azimuth was converted to crystal polar angle using the known experimental geometry. The relative degree of crystallinity (DoC) was calculated from these pole figures by integrating the intensities over the crystallographic orientation sphere: $\mathrm{DoC} = \int_{0°}^{90°} I(\omega) \sin \omega \, d\omega$. For the lamellar reflections, the intensities at the extreme ends of the measured range (ω = 1.5° and ω = 85°) were extended with polynomials to fill the missing regions. Because of the larger missing regions of intensity for the π-stacking pole figures, peak functions with constant backgrounds were fit to $I(\omega)$, similar to the procedure used in ref 47.

For measurements of the crystal spacing and coherence length, peak functions were fit to azimuthally averaged profiles $I(q)$. The azimuthal range for the averaging was selected on the basis of the dominant orientation of the crystal as measured by the pole figures, which corresponded to ±5° sector (wedge) profiles along the in- or out-of-plane scattering directions or, in the case of the lamellar diffraction from the as-cast IR film, the full azimuthal range. It should be noted that the absolute π-stacking coherence lengths were highly dependent on the chosen background but the relative values between samples remained consistent.

Transmission Electron Microscopy. TEM specimens were prepared by floating the polymer films in deionized water onto TEM copper grids with a holey carbon support film (C-Flat CF-22-2C, Protochips Inc., Raleigh, NC, USA). The carbon-coated copper grids were pretreated for 20 s by glow discharge. The polymer films immobilized on the TEM grids were dried at room temperature for at least 1 h. The specimens were inserted into sample holder (EM21010, JEOL GmbH, Eching, Germany) and transferred to a JEOL JEM-2100 transmission electron microscope with a LaB_6 cathode (JEOL GmbH, Eching, Germany). The microscope was operated at an acceleration voltage of 200 kV. All of the images were recorded digitally using a bottom-mounted 4k × 4k CMOS camera system (TemCam-F416, TVIPS, Gauting, Germany) and processed with a digital imaging processing system (EM-Menu 4.0, TVIPS, Gauting, Germany).

dx.doi.org/10.1021/ja4118736 | J. Am. Chem. Soc. 2014, 136, 4245−4256

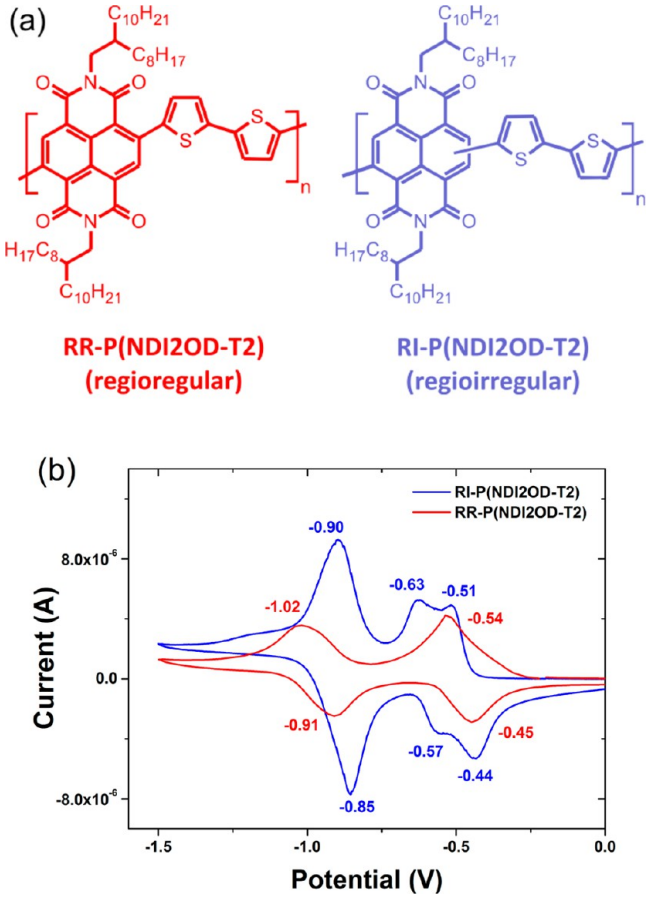

Figure 1. (a) Chemical structures of regioregular (RR) and regioirregular (RI) P(NDI2OD-T2). (b) Cyclic voltammograms of RR- and RI-P(NDI2OD-T2) referenced vs SCE.

RESULTS

Synthesis of RI-P(NDI2OD-T2). The synthesis of the regioregular polymer RR-P(NDI2OD-T2) (Figure 1a left) was straightforward[44] since the key polymer building block, *N*,*N*′-bis(2-octyldodecyl)-2,6-dibromonaphthalene-1,4,5,8-bis(dicarboximide) (NDI2OD-2,6Br_2), can be easily prepared from 2,6-dibromonaphthalene-1,4,5,8-bis(dicarboximide) (NDI-Br_2), a compound that can be obtained in excellent yields by brominating the corresponding anhydride (NDA). However, in order to obtain the regioirregular polymer RI-P(NDI2OD-T2) (Figure 1a right), it was necessary either to synthesize regiochemically pure *N*,*N*′-bis(2-octyldodecyl)-2,7-dibromonaphthalene-1,4,5,8-bis(dicarboximide) (NDI2OD-2,7Br_2) and mix it with NDI2OD-2,6Br_2 before polymerization with distannyldithiophene or to develop a synthetic path affording the mixture of the dibrominated NDI2OD isomers. Because of the great difficulties of the former approach, we designed and carried out a route affording the isomeric mixture as indicated in Scheme 1.

Details of the synthesis are reported in the Experimental Section. Briefly, NDA was tetrabrominated with DBI under strongly acidic conditions to afford NDA-Br_4 in good yield (94%), and NDA-Br_4 was then reacted with 2-octadecylamine to give NDI2OD-Br_4 as a pure solid after column chromatography on silica gel. Next, the tetrabromoimide system was subjected to random debromination using zinc powder, affording a mixture of brominated NDIs, from which a mixture of NDI2OD-2,6Br_2 (70%) and NDI2OD-2,7Br_2 (30%)

Scheme 1. Synthetic Route to the Regioirregular Polymer

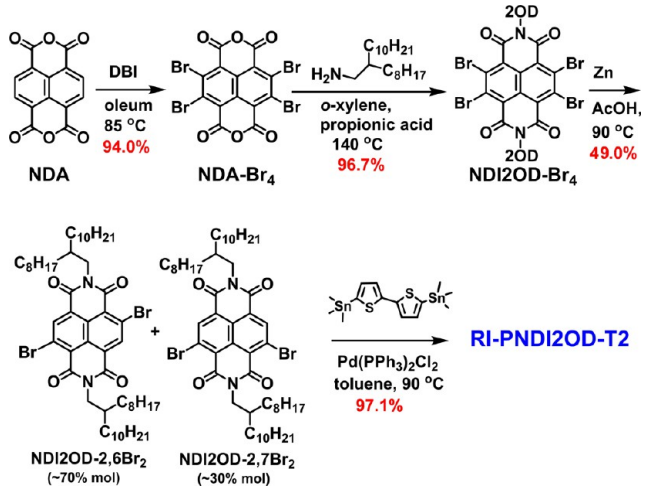

was isolated after column chromatography and multiple crystallizations. Finally, the regioirregular polymer was obtained by reacting the isomeric dibromide mixture with 5,5′-bis(trimethystannyl)-2,2′-dithiophene using $Pd(PPh_3)_2Cl_2$ as the catalyst. The new polymer was purified by multiple dissolution−precipitation procedures and was characterized by EA, GPC, and ^{1}H NMR spectroscopy. These systems are highly soluble in conventional organic solvents (e.g., >70 mg/mL in $CHCl_3$). The polymers used in this study had similar molecular weights and polydispersity indexes (PDIs): M_n = 28.6 kg/mol, M_w = 88.5 kg/mol, PDI = 3.1 for RI-P(NDI2OD-T2) and M_n = 29.3 kg/mol, M_w = 101.7 kg/mol, PDI = 3.5 for RR-P(NDI2OD-T2).

Electrochemical and Optical Properties. The LUMO energy of the RI polymer was determined by performing cyclic voltammetry on thin films as illustrated in Figure 1. RI-P(NDI2OD-T2) shows three reversible reduction peaks, with the first reduction [−0.48 V vs SCE, obtained by averaging the forward (−0.51 V) and reverse (−0.44 V) peaks] located at a voltage similar to that of the RR counterpart.[44] From this datum, the LUMO energy of RI-P(NDI2OD-T2) was calculated using the expression $E_{LUMO} = -(E_{1/2}^{red\text{-}1} + 4.44\ eV)$, which is based on the assumption that Koopmans' theorem holds ($EA^{red} \approx -E_{LUMO}$).[48] The LUMO energy was thus estimated as −3.96 eV, which is comparable to that of RR-P(NDI2OD-T2) (−3.94 eV). The difference in the shape of the first reduction feature for the RR and RI polymers can result either because the overlap of two reductions in the RR polymer leads to a broader single peak or because the presence of the regioirregular linkage (2,6 and 2,7) in RI-P(NDI2OD-T2) causes a different chemical environment around the NDI, leading to slightly different reduction features. As far as transport is concerned, however, the two peaks are very close in energy, so that the energetics of the LUMOs can be considered similar. This result, together with the optical absorption spectra of both polymers in chloronaphthalene (CN) solution (dashed lines in Figure 2a), indicates that the electronic structure of the unaggregated polymer chains is not strongly affected by the backbone regioirregularity.

In order to obtain films with different degrees of aggregation, we used our previously reported procedure, choosing as the solvent either chlorobenzene (CB), which promotes aggregation in solution, or a 1:1 (v/v) chloronaphthalene:xylene mixture (CN:Xyl), which prevents chain aggregation in

dx.doi.org/10.1021/ja4118736 | J. Am. Chem. Soc. 2014, 136, 4245−4256

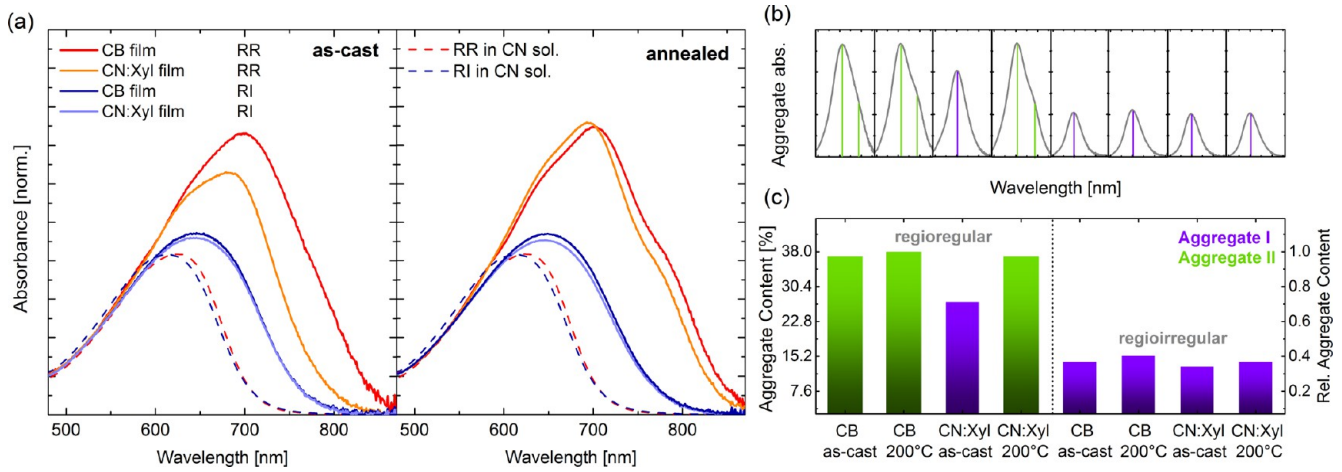

Figure 2. (a) Optical absorption spectra of RR-P(NDI2OD-T2) and RI-P(NDI2OD-T2) thin films spin-coated from the indicated solvents (CB = chlorobenzene, CN:Xyl = chloronaphthalene:xylene), as-cast and after annealing for 10 min at 200 °C. The absorption spectra of RR- and RI-P(NDI2OD-T2) in CN solution are reported using dashed lines and are representative of the absorption by the amorphous fraction. All of the spectra are normalized at 550 nm, where light absorption is due only to the unaggregated polymer chains.[32] (b) Deconvolution of the amorphous and aggregate absorption features, showing the absorption of the aggregate species for the different films obtained by removing the absorption of the amorphous content from the spectra in (a). The purple lines indicate the absorption peak at 700 nm of the aggregate I species, while the green lines indicate the absorption peaks at 710 and 790 nm of the aggregate II species. (c) Aggregate content and type for each of the analyzed films, obtained from the ratio of the amorphous and aggregate absorption intensities.

solution while maintaining sufficient wetting to the substrate as is essential for film deposition.[32,33] We prepared films with both RR- and RI-P(NDI2OD-T2) polymers, and we expected that the regioirregularity would reduce aggregation in solution regardless of the chosen solvent. All of the films were characterized both as-cast (dried in a vacuum oven at room temperature) and after annealing at 200 °C for 10 min in an inert atmosphere.

The optical absorption spectra of the RR- and RI-P(NDI2OD-T2) thin films obtained under different preparation conditions are reported as solid lines in Figure 2a. Similar to what is observed in solution (Figure S1 in the Supporting Information), RR-P(NDI2OD-T2) aggregation is strongly promoted in less polar solvents (going from CN to CB), leading to the formation of two different aggregate species, the first one absorbing only at ∼700 nm (aggregate I) and the second one exhibiting a main absorption at ∼710 nm and a shoulder at ∼790 nm (aggregate II).[32]

By deconvolution of the absorption spectra of the amorphous and aggregated species through removal of the contribution from the amorphous fraction of the film, which shows an unstructured absorption centered at ∼620 nm [dashed lines in Figure 2a, obtained from the spectra of P(NDI2OD-T2) in CN solution], it was possible to extract the absorption due to the aggregate species (reported in Figure 2b, following the method reported in ref 32). While it was impossible to separate analytically the absorption of the two aggregate types because of the considerable overlap of their spectra, we could determine the dominant aggregate type from the presence or absence of the absorption shoulder located at ∼790 nm. By comparison of the oscillator strengths of the amorphous and aggregate fractions in the film, it was also possible to obtain the aggregate content in each film (Figure 2c).[49]

All of the RR-P(NDI2OD-T2) films exhibit a considerable aggregate content (>25%), with the as-cast CN:Xyl film being the only one displaying exclusively aggregate I. This is consistent with the use of a solvent that inhibits aggregation. Thermal annealing (200 °C) of the films deposited either from CN:Xyl or from a solvent inducing preaggregation in solution (CB) leads to the formation of films dominated by aggregate II with a similar concentration (∼35% of the total mass), a value at which aggregation seems to saturate. Film annealing also induces a better definition of the aggregate absorption with the sharpening of the two absorption features. It should be noted that the aggregate content values reported here for RR-P(NDI2OD-T2) are slightly lower than those in our previous publication.[32] The absorption spectra presented in this work were measured more accurately using an integrating sphere, which removed the reflection and scattering contributions at long wavelengths.

The RI-P(NDI2OD-T2) films instead show a less structured absorption spectrum that is only slightly red-shifted compared with the one of the nonaggregated polymer in CN solution. More importantly, the presence of irregular links in the polymer backbone makes the optical spectra insensitive both to the solvent used for film deposition and to the annealing conditions. However after deconvolution of the amorphous and aggregate species, all of the RI-P(NDI2OD-T2) films still presented a significant fraction (15%) of aggregate I species, demonstrating that even this significant structural modification of the polymer backbone is not sufficient to completely prevent aggregation.

Despite the considerable shift of the optical band gap by over 100 nm (∼0.2 eV) in going from the RI- to the RR-P(NDI2OD-T2) film coated from CB, the LUMO energies obtained by cyclic voltammetry on solid layers showed no significant change. This result suggests that the optical shift is not caused by a further disruption of π-conjugation along the backbone of the RI polymer, as previously observed in going from RR- to RI-P3HT. For P3HT, head-to-head coupling twists the polymer backbone, affecting both the HOMO and LUMO topologies and energies.[39,40] The regioirregular coupling in RI-P(NDI2OD-T2), due to a change from meta to para linkage in the polymer backbone, does not introduce significant additional steric constraints on the backbone planarity since the 2,6- and

dx.doi.org/10.1021/ja4118736 | J. Am. Chem. Soc. 2014, 136, 4245−4256

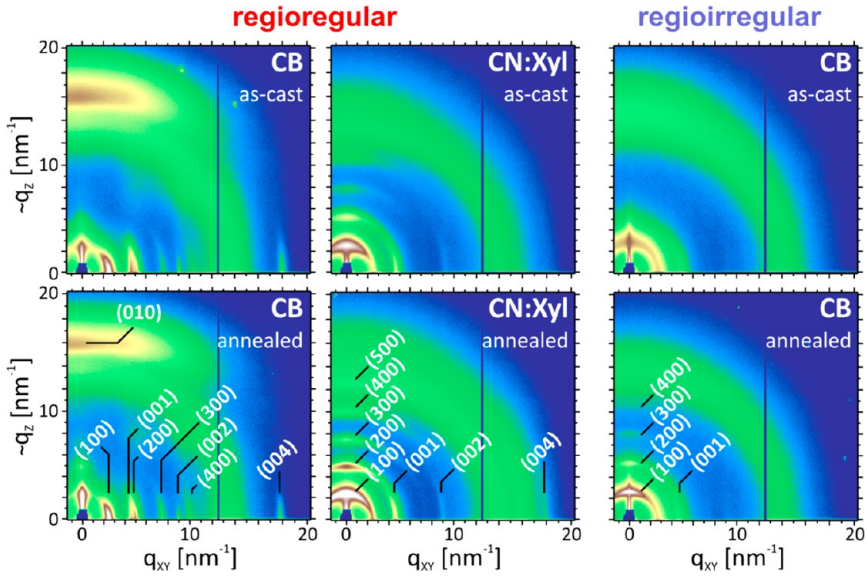

Figure 3. Plots of raw 2D GIXD detector intensities for the polymer films analyzed in this study. It should be noted that the q_Z values along the vertical axis are not accurate, being distorted by the curvature of the Ewald sphere. Geometrical corrections were applied for quantitative analysis in Figure 4. The peak assignments shown in the plots are based on previous reports.[26,38,50]

2,7-NDI–thiophene linkages have identical steric demand (identical local chemical connectivity). Furthermore, in this donor–acceptor copolymer the LUMO is strongly localized on the naphthalenediimide portion of the polymer, whereas the HOMO extends throughout the central portion of the polymer involving both the NDI and thiophene units.[23,25] Consequently, the specific chemical linkage should have a bigger impact on the HOMO localization compared to the LUMO.

Structural Characterization. To investigate and quantify the microstructures of the RR and RI polymer films, we characterized them using GIXD (Figure 3). Since the degree of aggregation of the RI-P(NDI2OD-T2) films was independent of the chosen solvent, we limited the analysis to films prepared from CB.

The GIXD plots demonstrate that the deposition solvent has a dramatic effect on the RR-P(NDI2OD-T2) film texture (crystal preferential orientation). With a more detailed inspection at the in-plane and out-of-plane diffraction patterns it is possible to observe that the (H00) diffraction peaks (due to lamellar stacking) are present out-of-plane ($\sim q_Z$ vector) for the CN:Xyl films and in-plane (q_{XY} vector) for the CB films; conversely, the (010) diffraction peak is observed in-plane for the CN:Xyl films and out-of-plane for the CB films. Therefore, while the crystalline fraction of the CN:Xyl films shows a preferential edge-on orientation (with the side chains aligned perpendicular to the substrate), the CB films are primarily oriented face-on with respect to the substrate surface [the (00L) peaks are observed in-plane in all of the plots, indicating that the side chains always lie parallel to the substrate]. Although it was not possible to determine the exact tilt angles of the NDI and T2 units from these measurements, they unambiguously identify the π-orbital stacking direction (parallel to the substrate for CN:Xyl and perpendicular to the substrate for CB). Thermal annealing at 200 °C, below the melting temperature, increases the crystalline phase content but preserves the orientation of the polymer chains in the crystallites. In the case of the annealed CB film, the diffraction peaks also show a change from arcs to rods, suggesting a long-range correlation of the crystallites having the same polymer orientation.[51] This change in microstructure when a different solvent is used gives access to films with similar thermal histories but different polymer orientations, allowing us to separately tune the degree of crystallinity and the polymer chain orientation.[38]

For the as-cast RI-P(NDI2OD-T2) films, a rather amorphous diffraction pattern is observed, although it is possible to discern the presence of a faint diffraction peak assignable to lamellar stacking oriented randomly with respect to the substrate. Upon thermal annealing, a significant intensity increase in the diffraction peak and the emergence of higher-order reflections indicate the formation of well-ordered stacks of polymer chains aligned perpendicular to the substrate (as for the RR films deposited from CN:Xyl), substantiating the results obtained from the optical spectra: despite the regioirregular linking between the donor and acceptor units, there is a consistent crystalline-phase fraction in the film.

The calculated pole figures for the first-order reflections along the lamellar- and π-stacking directions (Figure 4a)[52] represent the orientation distribution of the polymer crystals with respect to the surface normal after conversion of detector azimuth to crystal polar angle ω. The dramatic differences in crystal orientation for the regioregular polymer can easily be distinguished. Crystallites in the CB-cast films have almost exclusively face-on polymer chains, while the CN:Xyl-cast films exhibit a mainly edge-on chain orientation on top of a smaller, randomly oriented crystallite population. Thermal annealing increases the orientational preference in the CB-cast film, while the degree of crystallinity grows among all orientations in the CN:Xyl-cast film. The mirror relationship of the orientational preference between the lamellar and π-stacking indicates that the same crystallite population is being measured in each of the pole figures. For the RI-P(NDI2OD-T2) films, the pole figure for lamellar stacking indicates a completely randomized orientation of the packed chains in the as-cast sample, while thermal annealing seems to increase only the edge-on-oriented population. This result could indicate nucleation at one of the film interfaces or crystallization of a preexisting edge-on population of "amorphous" chains upon thermal annealing. In

dx.doi.org/10.1021/ja4118736 | J. Am. Chem. Soc. 2014, 136, 4245–4256

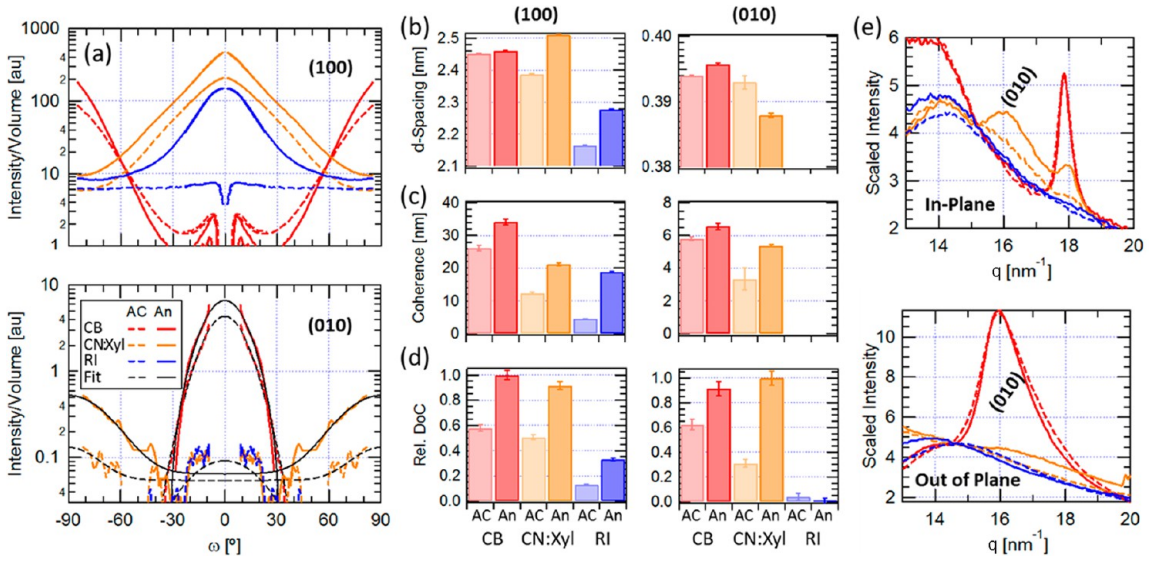

Figure 4. (a) Pole figures of the (top) (100) and (bottom) (010) peaks. (b–d) *d*-spacings, coherence lengths (2π/fwhm), and relative degrees of crystallinity (DoC) extracted from the first index peak for the lamellar (left) and π-stacking (right) directions. The uncertainties in (b) and (c) are the uncertainties in the unweighted fit parameters. The uncertainties in (d) are from uncertainties in the film thickness and sample length measurements. (e) Intensity-normalized (top) in-plane and (bottom) out-of-plane scattering profiles near the π-stacking diffraction peak at ~16.0 nm^{-1}. AC = as-cast, An = annealed.

contrast to the RR-P(NDI2OD-T2) films, while significant lamellar intensity is present in the pole figures of the regioirregular polymer film, no π-stacking intensity is observed. The small signal near ω = 0° is likely an artifact due to the assumption of a linear background. The extreme differences in crystal orientation with processing as well as the complete lack of π-stacking measured in the RI films is demonstrated in the profiles presented in Figure 4e.

The *d*-spacings in both the lamellar and π-stacking directions are reported in Figure 4b. The values measured for the RR polymer films are around 2.45 nm for the lamellar spacing and 0.39 nm for the π-stacking throughout the series, while the RI polymer films show a lower value of 2.20 nm for the lamellar spacing. Because of the missing π-stacking peak in the RI films, no information on the packing along this direction could be obtained. The coherence lengths along the different directions (Figure 4c) show a more significant dependence on the processing conditions, with crystallites growing along both the π- and lamellar-stacking directions when CB was used instead of CN:Xyl and upon annealing. It is very interesting to note how the RI-P(NDI2OD-T2) films, when annealed, show a coherence length of the lamellar stacking comparable to that of the annealed CN:Xyl film (20 nm), indicating the formation of large, coherent lamellae despite the irregular backbone. The lamellar *d* spacing also shows a general tendency to increase with the increased ordering in the film, whereas the π-stacking does not. The DoCs extracted from the pole plots following the procedure reported in the Experimental Section (Figure 4d) show similar crystallinity enhancements along the two directions, indicating that crystallite growth proceeds along both directions. The plots also clearly show the role of annealing in increasing the crystalline fraction for both the RR and RI polymer films. The parameters obtained for the backbone diffraction peaks follow a very similar trend as those for the lamellar stacking peak, except for the DoC, which was found to be constant for all of the films (Figure S2 in the Supporting Information).

Transmission Electron Microscopy Analysis. TEM allows for a closer view of the layer morphology for the different orientations of the RR-P(NDI2OD-T2) polymer chains (Figure 5). In the low-magnification image of the CB film (Figure 5a), the periodic structure of the stacked chains is clearly visible, while for the CN:Xyl film (Figure 5d) it is not possible to distinguish any feature. In the inset of these two images, the Fourier transforms of the images are shown. In the CB case, two perpendicular features with *q* vectors compatible with the (100) and (001) peaks obtained with GIXD can be observed, thus confirming the face-on configuration of the polymer chains. Furthermore, the crystalline domains seem to be highly interconnected and share a long-range order on a micrometer scale, as also shown for the face-on orientation in the work of Takacs et al.[53] and as indicated also from the rod-shaped diffraction peaks. The fast Fourier transform analysis of the CN:Xyl film shows instead only one feature, consistent with the (010) peak of the π-stacking, and a much stronger amorphous halo. At intermediate magnification (Figure 5b,e) it is easier to notice how the structure observed in the face-on films is absent from the edge-on films, and only by magnifying the CN:Xyl film image further (Figure 5f) and removing the amorphous content via Fourier filtering is it possible to observe the structure due to the π-stacking of the polymer chains, edge-on relative to the substrate. We finally notice that a rough estimate of the crystalline fraction obtained from the TEM image (shaded areas in Figure 5b) is consistent with the aggregate fraction determined from the optical measurements.

Aggregation versus Crystallization. The comparison between the optical and X-ray measurements provides interesting insights on the interplay between polymer aggregation and thin-film crystallinity. Let us first consider the most local parameters, the backbone (001) coherence length and the degree of aggregation. The first parameter is approximately the average length of straight-chain segments, while the second measures the fraction of chains that exhibit red-shifted aggregate absorption. It has been shown previously that this red shift originates mainly from a change in backbone

dx.doi.org/10.1021/ja4118736 | J. Am. Chem. Soc. 2014, 136, 4245–4256

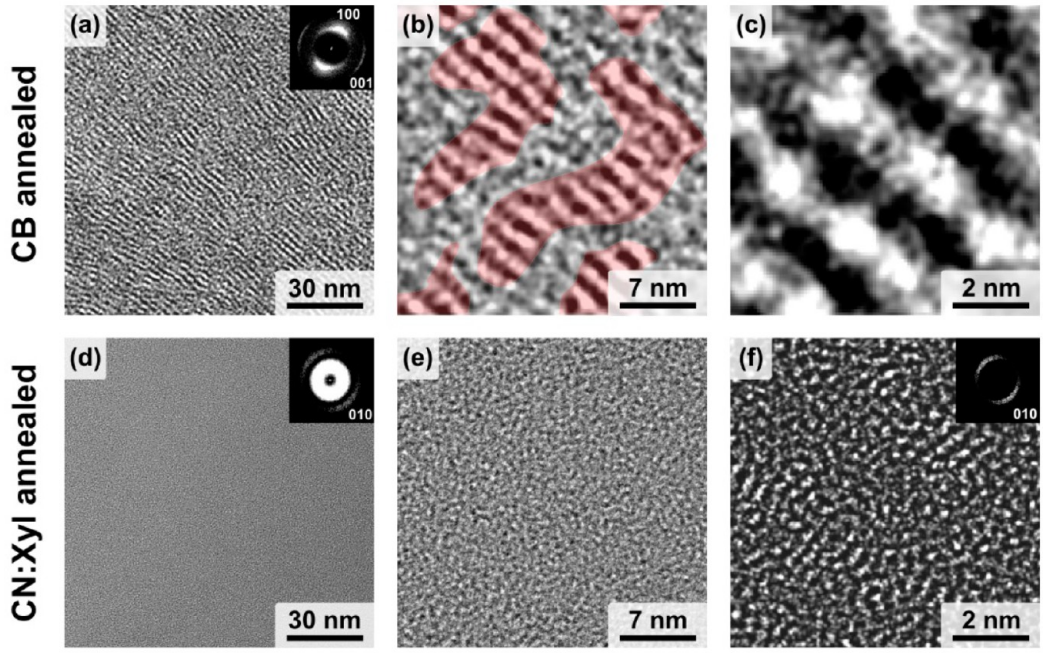

Figure 5. TEM images of RR-P(NDI2OD-T2) prepared from CB and 1:1 (v/v) CN:Xyl after annealing. (a) Low-magnification image of the CB film, which shows the aligned polymer chains lying face-on. The Fourier transform of the image, in the inset, shows two periodic features corresponding to the (100) and the (001) stacking directions. (b) Close-up of the image in (a), showing the aligned polymer chains. The periodic structures correspond to roughly 46% of the area of the image. (c) High-magnification image showing the stacked polymer chains. (d) Low-magnification image of the CN:Xyl film, where no features can be distinguished. The Fourier transform, in the inset, allows the detection of a faint periodic feature with a characteristic length corresponding to the π-stacking. (e) Close-up of the image in (d), showing the difference in packing with respect to the CB film. In order to resolve the underlying periodic structure, it was necessary to filter the amorphous contribution using the Fourier transform and go to higher magnification (f), where it was possible to observe the edge-on configuration on the substrate surface.

conformation induced by interchain interactions in π-stacked multichain assemblies.[32] We observe a strict correlation between the (001) coherence length and the degree of aggregation (DoA) (Figure S3 in the Supporting Information). In view of the fact that chain straightening facilitates intimate contact between neighboring chains and, vice versa, interchain interactions enforce a linear chain conformation, the observed correlation is highly meaningful.

Since straight-chain segments and strong $\pi-\pi$ interactions are inevitable for extended ordering in the π-stacking direction, samples with low (001) coherence and small DoAs also exhibit low (010) DoCs and coherence. This correlation is less strict when considering the lamellar ordering. It is possible that the presence of long, flexible side chains levels out the backbone distortion to a certain extent.

The comparison of Figure 4d and Figure 2c also reveals that the increase in DoC with annealing is stronger than the corresponding increase in DoA. This is most obvious for the CB-cast sample, which exhibits similar DoAs in the as-cast and annealed films, while annealing causes the DoC in the (100) and (010) directions to approximately double. This suggests a role for the aggregates as initiators for the formation of crystallites and that the crystallinity increase proceeds through the alignment and coalescence of multiple aggregates.

Despite the importance of aggregates for crystal formation, there is no trivial relation between the structural parameters of the crystallites as inferred from wide-angle X-ray scattering data and the assignment of the optical aggregate species type. While Figure 2 displays two very distinct absorption features, which we assign to aggregate I or aggregate II, no such unique features are seen in the X-ray data. Instead, we observe a gradual increase of the (H00) and (00L) spacings with increasing order, while no clear correlation with order is seen for the (0K0) spacing. Lemaur et al.[54] calculated the change in d-spacing along the (100) direction and explained it in terms of a change in interdigitation of the side chains, which in our case could suggest a change in conformation of the polymer chains with a change in the preparation conditions. However it is difficult to detect the different conformers from the d-spacing along the lamellar stacking direction only, and the changes do not correlate directly with the different aggregate types.

It has also been shown for RR-P(NDI2OD-T2) that it is possible to induce two different polymorphs, denoted as form I and form II. In form I, adjacent chains show a segregated structure [with donor (acceptor) units stacking on top of each other], while form 2 has a mixed structure (with donor units stacking on top of the acceptor units of the adjacent chain).[55] Despite very similar d-spacings in all three crystallographic directions, these two forms could be identified well by their different 001-to-002 intensity ratios, with the mixed structure (form II) exhibiting a highly suppressed 001 diffraction. All of our samples, including those of RI-P(NDI2OD-T2), have similar 001-to-002 intensity ratios, with the 001 peak being more intense, meaning that they mainly consist of chains with the segregated packing (form I).

We therefore propose that the optical properties of the two aggregate species are determined mainly by the backbone conformation, most likely the tilt angle between the donor and acceptor units. It is in fact known from quantum-chemical calculations that the low-energy absorption peak is due to an excitation from the HOMO (localized on the bithiophene unit) to the LUMO (localized on the NDI unit)[23] with a strong

dx.doi.org/10.1021/ja4118736 | J. Am. Chem. Soc. 2014, 136, 4245−4256

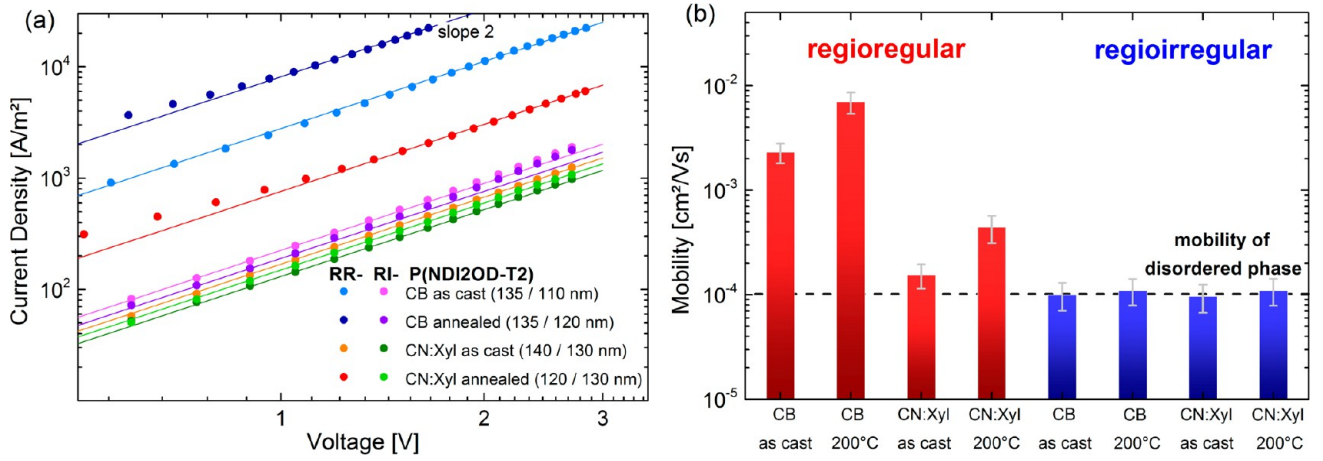

Figure 6. (a) $J-V$ characteristics (for clarity, only one every three data points is shown) of electron-only diodes with RR- and RI-P(NDI2OD-T2). The films spun from chlorobenzene show the highest conductivity, while the chloronaphthalene:xylene ones exhibit worse performance. The lines are fits to the experimental data using the standard trap-free SCLC equation with a fixed slope of 2, as expected from the quadratic dependence of the current on the applied voltage. (b) Mobilities extracted using the SCLC formalism. Values obtained with the regioirregular polymer are shown in blue, while the results obtained with the regioregular one are shown in red. Error bars were obtained by averaging several devices on each substrate and taking into account the uncertainty in the thickness measurements.

charge transfer character. It has also been shown that for RR-P(NDI2OD-T2) there are two stable configurations for the relative orientation of the donor and acceptor in the polymer repeating unit,[28,56] one with a dihedral tilt angle of 42° and a slightly more energetically stable one with a tilt angle of 138°. This is consistent with the results we reported for calculations of the optical transitions performed on aggregated P(NDI2OD-T_2) oligomers, which showed a considerable red shift of the charge transfer transition due to a reduction of just 10° in the dihedral angle between the donor and the acceptor units in the polymer chains.[32] The change in dihedral angle between the donor and the acceptor units in the monomer was also observed in the work by Lemaur, where the several stable packing structures display different tilt angles between the donor and acceptor. These results indicate that a change in the dihedral angle between the donor and acceptor units of the monomer in an ordered stack of the polymer chains could be responsible for the changes in the absorption spectra of the different films. This result would also explain the similar LUMO energies for the RR and RI polymers, as the regioirregular linkage would not hinder delocalization of the LUMO. This is seen by the appearance of lamellar stacking with a coherence length as large as 20 nm in the annealed layer of RI-P(NDI2OD-T2), which necessitates that the NDI units can adopt a regular conformation following the strong tendency toward interdigitation of the side chains. On the other hand, because of the regioirregular linkage, the bithiophene units will always show random tilt angles with respect to the NDI unit, which will strongly affect the HOMO and limit aggregation of neighboring polymer chains in RI-P(NDI2OD-T2) while still allowing the NDI units of subsequent repeat units to exhibit the same orientation. The reason for the formation of only aggregate I in the regioirregular polymer, despite the fact that aggregate II is thermodynamically favorable, might be connected to the longer correlation length along the polymer backbone observed in the regioregular polymer, which might be required for the stabilization of the HOMO, meaning that such stabilization could not be achieved in the regioirregular polymer.

Electrical Characterization. The possibility of tuning the polymer chain orientation upon solvent selection, combined with the knowledge of the microstructure of the films fabricated with different conditions, and the availability of both the RR and RI polymers enables us to disentangle the role of each parameter affecting the charge transport properties of P-(NDI2OD-T2). In particular, RI-P(NDI2OD-T2) allows us to analyze for the first time a system that shows a very anisotropic crystallization, large and well-defined lamellar stacking, and undetectable π-stacking, therefore also allowing us to address the anisotropic charge transport function of the degree of ordering along the different crystallographic directions.

In order to extract the electron mobility, we realized space-charge-limited current (SCLC) diodes with the same preparation conditions as for the films used for the structural characterization. The current density−voltage ($J-V$) characteristics for these devices are reported in Figure 6a [the full $J-V$ characteristics, including the low-voltage part of the plot which shows Ohmic behavior, are shown in Figure S4 in the Supporting Information for devices prepared from RR-P(NDI2OD-T2)]. As can be seen from the plot, all of the curves show a quadratic dependence of the current density on the applied voltage for most of the voltage range. While we originally showed that electron injection into RR-P(NDI2OD-T2) from typical cathodes (Ca, Ba, Sm, and CsF) is contact-limited,[31] Wetzelaer et al.[28] recently demonstrated Ohmic injection for this material by using cesium carbonate as the top contact. Inspired by this work, we used Cs_2CO_3 as the top and bottom contacts in order to prevent the oxidation of the bottom aluminum electrode upon heat treatment.

The SCLC mobilities μ were extracted using the standard trap-free SCLC transport equation:

$$J = \frac{9}{8}\varepsilon_r\varepsilon_0\mu\frac{U^2}{d^3}$$

where ε_r is the relative dielectric constant, ε_0 is the vacuum permeability, U is the applied voltage, and d is the device thickness. The validity of the extraction method was confirmed by ensuring that the current across devices with different thicknesses scaled according to a d^{-3} dependence (Figure S5 in

dx.doi.org/10.1021/ja4118736 | J. Am. Chem. Soc. 2014, 136, 4245−4256

the Supporting Information). The extracted mobilities are reported in Figure 6b.

The most obvious correlation is between chain orientation and mobility. Notably, though the pristine CB-coated RR sample with face-on orientation has a lower DoC in the lamellar and π-stacking directions, the mobility of this film is almost 10 times higher than that of the annealed CN:Xy-cast film with an edge-on morphology. This confirms the importance of coherent π-stacking along the direction of charge transport for reaching extraordinarily high electron mobilities with this polymer. The 3-fold increase in mobility upon annealing of the CB-coated sample is correlated with the increase in DoC, indicating the formation of more or larger crystalline domains from the aggregate species. Interestingly, annealing the edge-on-oriented samples also results in an approximate 3-fold increase in mobility. While one might be tempted to attribute this simply to the transition from aggregate I to aggregate II, we notice the large increase in both the DoC and the coherence length along the π-stacking direction upon annealing. The concurrent improvement of in-plane transport provides better access to pathways for charge transport along the vertical direction.[57] Our proposal is that the π-stacking coherence and not the quality of packing in the lamellar direction is important for efficient vertical transport also in the case of edge-on chain orientation.

This view is fully confirmed by the electrical properties of RI-P(NDI2OD-T2). Despite the fact that annealing leads to a considerable increase in the coherence length and DoC in the lamellar direction of that sample, the vertical mobility is not affected. In view of the lack of any order along the π-stacking direction, this result is a clear indication of how the increase in coherence length and DoC along the lamellar stacking direction has no impact on the electron transport properties.

Finally, we note that even the as-cast RI-P(NDI2OD-T2) film, which has a very low DoC in any direction, shows a surprisingly high mobility compared with other regioirregular polymers such as RI-P3HT.[12,58] In particular, a close look at the shape of the SCLC curves reveals a clear quadratic dependence for all of the different devices, with both the RR and RI polymers. The similarity of the different traces indicates that apart from a general decrease in the the electron mobility, the energetic landscape is very similar for RR- and RI-P(NDI2OD-T2) and characterized also in the more amorphous films by a very small energetic disorder.[59]

This corroborates the hypothesis that the LUMO is not strongly changed upon aggregation, as already discussed in the previous section, so that while charge transfer is enhanced by the increase of DoC along the π-stacking direction, the energetic structure of the LUMO is not. The reason is twofold. The regiorandom coupling in P3HT has a direct impact on the conjugation length due to steric constraints, as it inhibits planarization of the backbone, thus dramatically affecting the energetic structure of the polymer film. This is not true for the regiorandom coupling in P(NDI2OD-T2), where the irregular linking does not cause the same steric hindrance issues. For the latter polymer, the main effect seems to be related to the inhibition of π-stacking, while the LUMO energy is not strongly affected by the presence of irregular linking, as shown from the electrochemical data. Moreover, according to quantum-chemical calculations, negative charges in P(NDI2OD-T2) are delocalized over a small number of repeating units compared to polymers such as P3HT.[23] Combined with the larger and more planar repeating units adopted in this high-mobility polymer, this leads to a structure that is more tolerant of disorder and provides a higher baseline for charge transport regardless of the film microstructure.[60]

CONCLUSIONS

Analyzing and comparing the optical, structural, and charge transport information, this work shows some peculiar properties of semiconducting donor−acceptor NDI copolymers. In order to study the role of solid-state morphology and microstructure on the charge transport properties of regioregular P(NDI2OD-T2), we prepared thin films using different solvents to tune the degree of aggregation in solution. Structural characterization of the thin films revealed that the different solvents have a dramatic impact on the orientation of the polymer chains with respect to the substrate, allowing us to achieve edge-on and face-on microstructured films without thermal annealing of the polymer films above the melting temperature.

Measuring the vertical electron mobility in unipolar diodes revealed that crystallinity along the π-stacking direction is highly important for achieving high electron mobilities. On the other hand, the side chains create a barrier for electron transfer, demonstrating how lamellar ordering plays little role in electron transport. The anisotropy of the charge transport properties was confirmed by the effect of chain orientation in the RR polymer films, where vertical diodes comprising films with the face-on morphology display a one order of magnitude increase in electron mobility compared with diodes prepared from films having an edge-on polymer conformation.

We have also reported a new synthetic route to obtain a regioirregular version of P(NDI2OD-T2), which shows a similar LUMO energy as the regioregular counterpart but a lower degree of aggregation, which however still involves ∼10% of the total polymer mass. Surprisingly, this polymer shows an anisotropic packing structure with the formation of well-ordered lamellar stacks but without measurable π-stacking. Furthermore, our results indicate that the irregular linkage does not increase the backbone steric demand between the large NDI units despite the random orientation of the bithiophene units. This is different from regioirregular P3HT, where the different absorption and much lower mobility compared with regioregular P3HT have been attributed to steric constraints. As a consequence, we observed a rather moderate difference in mobility between RR- and RI-P(NDI2OD-T2). This study demonstrates how the use of larger planar units can indeed improve the charge transfer process, making it more resilient to the increased disorder introduced by the regioirregular linking and providing a higher baseline mobility regardless of the microstructure of the polymer film.

ASSOCIATED CONTENT

Supporting Information

Spectra of RR- and RI-P(NDI2OD-T2) in different solvents (Figure S1); analysis of the backbone diffraction peaks (Figure S2); correlation between the backbone diffraction peak coherence length and aggregate content (Figure S3); full $J-V$ plots, including the Ohmic part of the curves (Figure S4); and thickness dependence of the SCLC curves (Figure S5). This material is available free of charge via the Internet at http://pubs.acs.org.

AUTHOR INFORMATION

Corresponding Authors

a-facchetti@northwestern.edu
neher@uni-potsdam.de

Notes

The authors declare no competing financial interest.

ACKNOWLEDGMENTS

F.P. thanks the CRC 951 of the Deutsche Forschungsgemeinschaft (DFG) and the Joint Lab for Structural Research Berlin for funding. M.S. acknowledges funding by the DFG within the SPP 1355. B.A.C. acknowledges financial support from the NIST-NRC Postdoctoral Fellowship Program. H.A. was supported by DOE, OS, BES, MSE (DE-FG02-98ER45737). GIXD data were acquired at beamline 7.3.3 of the Advanced Light Source, a National User Facility supported by DOE (DE-AC02-05CH1123). Part of this work was funded by the German Federal Ministry of Science and Education (BMBF FKZ 03X3525D) within SOHyb (FKZ 03X3525D). D.N. thanks the DFG for a travel grant. This work was financially supported by the Deutsche Forschungsgemeinschaft (DFG) within the Collaborative Research Centre HIOS (SFB 951).The authors acknowledge Gert-Jan Wetzelaer and Jan-Anton Koster for help in the preparation of the SCLC diodes used in this work and Dr. Holm Kirmse for fruitful discussion concerning the TEM results.

REFERENCES

(1) Donley, C. L.; Zaumseil, J.; Andreasen, J. W.; Nielsen, M. M.; Sirringhaus, H.; Friend, R. H.; Kim, J. *J. Am. Chem. Soc.* **2005**, *127*, 12890−12899.

(2) Salleo, A. *Mater. Today* **2007**, *10*, 38−45.

(3) McCulloch, I.; Heeney, M.; Bailey, C.; Genevicius, K.; Macdonald, I.; Shkunov, M.; Sparrowe, D.; Tierney, S.; Wagner, R.; Zhang, W.; Chabinyc, M. L.; Kline, R. J.; McGehee, M. D.; Toney, M. F. *Nat. Mater.* **2006**, *5*, 328−333.

(4) Cadby, A. J.; Lane, P. A.; Mellor, H.; Martin, S. J.; Grell, M.; Giebeler, C.; Bradley, D. D. C.; Wohlgenannt, M.; An, C.; Vardeny, Z. V. *Phys. Rev. B* **2000**, *62*, 15604−15609.

(5) Guo, X.; Zhou, N.; Lou, S. J.; Smith, J.; Tice, D. B.; Hennek, J. W.; Ortiz, R. P.; Navarrete, J. T. L.; Li, S.; Strzalka, J.; Chen, L. X.; Chang, R. P. H.; Facchetti, A.; Marks, T. J. *Nat. Photonics* **2013**, *7*, 815−833.

(6) Facchetti, A. *Chem. Mater.* **2011**, *23*, 733−758.

(7) Sirringhaus, H.; Brown, P. J.; Friend, R. H.; Nielsen, M. M.; Bechgaard, K.; Langeveld-Voss, B. M. W.; Spiering, A. J. H.; Janssen, R. A. J.; Meijer, E. W.; Herwig, P.; de Leeuw, D. M. *Nature* **1999**, *401*, 685−688.

(8) Zen, A.; Pflaum, J.; Hirschmann, S.; Zhuang, W.; Jaiser, F.; Asawapirom, U.; Rabe, J. P.; Scherf, U.; Neher, D. *Adv. Funct. Mater.* **2004**, *14*, 757−764.

(9) Kline, R. J.; McGehee, M. D.; Kadnikova, E. N.; Liu, J.; Fréchet, J. M. J. *Adv. Mater.* **2003**, *15*, 1519−1522.

(10) Jimison, L. H.; Toney, M. F.; McCulloch, I.; Heeney, M.; Salleo, A. *Adv. Mater.* **2009**, *21*, 1568−1572.

(11) Sirringhaus, H.; Tessler, N.; Friend, R. H. *Science* **1998**, *280*, 1741−1744.

(12) Bao, Z.; Dodabalapur, A.; Lovinger, A. J. *Appl. Phys. Lett.* **1996**, *69*, 4108−4110.

(13) Crossland, E. J. W.; Tremel, K.; Fischer, F.; Rahimi, K.; Reiter, G.; Steiner, U.; Ludwigs, S. *Adv. Mater.* **2012**, *24*, 839−844.

(14) Luzio, A.; Fazzi, D.; Natali, D.; Giussani, E.; Baeg, K.-J.; Chen, Z.; Noh, Y.-Y.; Facchetti, A.; Caironi, M. *Adv. Funct. Mater.* **2013**, DOI: 10.1002/adfm.201302297.

(15) Chen, H.; Guo, Y.; Yu, G.; Zhao, Y.; Zhang, J.; Gao, D.; Liu, H.; Liu, Y. *Adv. Mater.* **2012**, *24*, 4618−4622.

(16) Chen, Z.; Lee, M. J.; Shahid Ashraf, R.; Gu, Y.; Albert-Seifried, S.; Nielsen, M. M.; Schroeder, B.; Anthopoulos, T. D.; Heeney, M.; McCulloch, I.; Sirringhaus, H. *Adv. Mater.* **2012**, *24*, 647−652.

(17) Van Hal, P. A.; Smits, E. C. P.; Geuns, T. C. T.; Akkerman, H. B.; De Brito, B. C.; Perissinotto, S.; Lanzani, G.; Kronemeijer, A. J.; Geskin, V.; Cornil, J.; Blom, P. W. M.; De Boer, B.; De Leeuw, D. M. *Nat. Nanotechnol.* **2008**, *3*, 749−754.

(18) Kronemeijer, A. J.; Gili, E.; Shahid, M.; Rivnay, J.; Salleo, A.; Heeney, M.; Sirringhaus, H. *Adv. Mater.* **2012**, *24*, 1558−1565.

(19) Tsao, H. N.; Cho, D. M.; Park, I.; Hansen, M. R.; Mavrinskiy, A.; Yoon, D. Y.; Graf, R.; Pisula, W.; Spiess, H. W.; Müllen, K. *J. Am. Chem. Soc.* **2011**, *133*, 2605−2612.

(20) Lu, G.; Blakesley, J.; Himmelberger, S.; Pingel, P.; Frisch, J.; Lieberwirth, I.; Salzmann, I.; Oehzelt, M.; Di Pietro, R.; Salleo, A.; Koch, N.; Neher, D. *Nat. Commun.* **2013**, *4*, No. 1588.

(21) Zhang, X.; Bronstein, H.; Kronemeijer, A. J.; Smith, J.; Kim, Y.; Kline, R. J.; Richter, L. J.; Anthopoulos, T. D.; Sirringhaus, H.; Song, K.; Heeney, M.; Zhang, W.; McCulloch, I.; DeLongchamp, D. M. *Nat. Commun.* **2013**, *4*, No. 2238.

(22) Yan, H.; Chen, Z.; Zheng, Y.; Newman, C.; Quinn, J. R.; Dötz, F.; Kastler, M.; Facchetti, A. *Nature* **2009**, *457*, 679−686.

(23) Caironi, M.; Bird, M.; Fazzi, D.; Chen, Z.; Di Pietro, R.; Newman, C.; Facchetti, A.; Sirringhaus, H. *Adv. Funct. Mater.* **2011**, *21*, 3371−3381.

(24) Baeg, K.-J.; Khim, D.; Jung, S.-W.; Kang, M.; You, I.-K.; Kim, D.-Y.; Facchetti, A.; Noh, Y.-Y. *Adv. Mater.* **2012**, *24*, 5433−5439.

(25) Fazzi, D.; Caironi, M.; Castiglioni, C. *J. Am. Chem. Soc.* **2011**, *133*, 19056−19059.

(26) Rivnay, J.; Toney, M. F.; Zheng, Y.; Kauvar, I. V.; Chen, Z.; Wagner, V.; Facchetti, A.; Salleo, A. *Adv. Mater.* **2010**, *22*, 4359−4363.

(27) Schuettfort, T.; Thomsen, L.; McNeill, C. R. *J. Am. Chem. Soc.* **2013**, *135*, 1092−1101.

(28) Wetzelaer, G.-J. A. H.; Kuik, M.; Olivier, Y.; Lemaur, V.; Cornil, J.; Fabiano, S.; Loi, M. A.; Blom, P. W. M. *Phys. Rev. B* **2012**, *86*, No. 165203.

(29) Fabiano, S.; Musumeci, C.; Chen, Z.; Scandurra, A.; Wang, H.; Loo, Y.-L.; Facchetti, A.; Pignataro, B. *Adv. Mater.* **2012**, *24*, 951−956.

(30) Fabiano, S.; Yoshida, H.; Chen, Z.; Facchetti, A.; Loi, M. A. *ACS Appl. Mater. Interfaces* **2013**, *5*, 4417−4422.

(31) Steyrleuthner, R.; Schubert, M.; Jaiser, F.; Blakesley, J. C.; Chen, Z.; Facchetti, A.; Neher, D. *Adv. Mater.* **2010**, *22*, 2799−2803.

(32) Steyrleuthner, R.; Schubert, M.; Howard, I.; Klaumünzer, B.; Schilling, K.; Chen, Z.; Saalfrank, P.; Laquai, F.; Facchetti, A.; Neher, D. *J. Am. Chem. Soc.* **2012**, *134*, 18303−18317.

(33) Schubert, M.; Dolfen, D.; Frisch, J.; Roland, S.; Steyrleuthner, R.; Stiller, B.; Chen, Z.; Scherf, U.; Koch, N.; Facchetti, A.; Neher, D. *Adv. Energy Mater.* **2012**, *2*, 369−380.

(34) Facchetti, A. *Mater. Today* **2013**, *16*, 123−132.

(35) Zhou, N.; Lin, H.; Lou, S. J.; Yu, X.; Guo, P.; Manley, E. F.; Loser, S.; Hartnett, P.; Huang, H.; Wasielewski, M. R.; Chen, L. X.; Chang, R. P. H.; Facchetti, A.; Marks, T. J. *Adv. Energy Mater.* **2013**, DOI: 10.1002/aenm.201300785.

(36) Tang, Y.; McNeill, C. R. *J. Polym. Sci., Part B: Polym. Phys.* **2013**, *51*, 403−409.

(37) Mori, D.; Benten, H.; Okada, I.; Ohkita, H.; Ito, S. *Adv. Energy Mater.* **2013**, DOI: 10.1002/aenm.201301006.

(38) Rivnay, J.; Steyrleuthner, R.; Jimison, L. H.; Casadei, A.; Chen, Z.; Toney, M. F.; Facchetti, A.; Neher, D.; Salleo, A. *Macromolecules* **2011**, *44*, 5246−5255.

(39) Ko, S.; Hoke, E. T.; Pandey, L.; Hong, S.; Mondal, R.; Risko, C.; Yi, Y.; Noriega, R.; McGehee, M. D.; Brédas, J.-L.; Salleo, A.; Bao, Z. *J. Am. Chem. Soc.* **2012**, *134*, 5222−5232.

(40) Tsoi, W. C.; Spencer, S. J.; Yang, L.; Ballantyne, A. M.; Nicholson, P. G.; Turnbull, A.; Shard, A. G.; Murphy, C. E.; Bradley, D. D. C.; Nelson, J.; Kim, J.-S. *Macromolecules* **2011**, *44*, 2944−2952.

(41) Wang, C.; Rivnay, J.; Himmelberger, S.; Vakhshouri, K.; Toney, M. F.; Gomez, E. D.; Salleo, A. *ACS Appl. Mater. Interfaces* **2013**, *5*, 2342−2346.

(42) Letizia, J. A.; Salata, M. R.; Tribout, C. M.; Facchetti, A.; Ratner, M. A.; Marks, T. J. *J. Am. Chem. Soc.* **2008**, *130*, 9679−9694.
(43) Goto, H.; Akagi, K. *Angew. Chem., Int. Ed.* **2005**, *44*, 4322−4328.
(44) Chen, Z.; Zheng, Y.; Yan, H.; Facchetti, A. *J. Am. Chem. Soc.* **2009**, *131*, 8−9.
(45) Röger, C.; Würthner, F. *J. Org. Chem.* **2007**, *72*, 8070−8075.
(46) Hexemer, A.; Bras, W.; Glossinger, J.; Schaible, E.; Gann, E.; Kirian, R.; MacDowell, A.; Church, M.; Rude, B.; Padmore, H. *J. Phys.: Conf. Ser.* **2010**, *247*, No. 012007.
(47) Duong, D. T.; Toney, M. F.; Salleo, A. *Phys. Rev. B* **2012**, *86*, No. 205205.
(48) Bard, A. J.; Faulkner, L. R. *Electrochemical Methods: Fundamentals and Applications*; Wiley: New York, 1980.
(49) Clark, J.; Chang, J.-F.; Spano, F. C.; Friend, R. H.; Silva, C. *Appl. Phys. Lett.* **2009**, *94*, No. 163306.
(50) Rivnay, J.; Noriega, R.; Kline, R. J.; Salleo, A.; Toney, M. F. *Phys. Rev. B* **2011**, *84*, No. 045203.
(51) Himmelberger, S.; Dacuña, J.; Rivnay, J.; Jimison, L. H.; McCarthy-Ward, T.; Heeney, M.; Toney, M. F.; Salleo, A. *Adv. Funct. Mater.* **2013**, *23*, 2091−2098.
(52) Baker, J. L.; Jimison, L. H.; Mannsfeld, S.; Volkman, S.; Yin, S.; Subramanian, V.; Salleo, A.; Alivisatos, A. P.; Toney, M. F. *Langmuir* **2010**, *26*, 9146−9151.
(53) Takacs, C. J.; Treat, N. D.; Kraemer, S.; Chen, Z.; Facchetti, A.; Chabinyc, M. L.; Heeger, A. J. *Nano Lett.* **2013**, *13*, 2522−2527.
(54) Lemaur, V.; Muccioli, L.; Zannoni, C.; Beljonne, D.; Lazzaroni, R.; Cornil, J.; Olivier, Y. *Macromolecules* **2013**, *46*, 8171−8178.
(55) Brinkmann, M.; Gonthier, E.; Bogen, S.; Tremel, K.; Ludwigs, S.; Hufnagel, M.; Sommer, M. *ACS Nano* **2012**, *6*, 10319−10326.
(56) Giussani, E.; Fazzi, D.; Brambilla, L.; Caironi, M.; Castiglioni, C. *Macromolecules* **2013**, *46*, 2658−2670.
(57) Tessler, N.; Preezant, Y.; Rappaport, N.; Roichman, Y. *Adv. Mater.* **2009**, *21*, 2741−2761.
(58) Assadi, A.; Svensson, C.; Willander, M.; Inganäs, O. *Appl. Phys. Lett.* **1988**, *53*, 195−197.
(59) Nicolai, H. T.; Mandoc, M.; Blom, P. W. M. *Phys. Rev. B* **2011**, *83*, No. 195204.
(60) Noriega, R.; Rivnay, J.; Vandewal, K.; Koch, F. P. V.; Stingelin, N.; Smith, P.; Toney, M. F.; Salleo, A. *Nat. Mater.* **2013**, *12*, 1038−1044.